Available online at www.sciencedirect.com
ScienceDirect
Trans. Nonferrous Met. Soc. China 34(2024) 1413−1426
Transactions of Nonferrous Metals Society of China
www.tnmsc.cn

# Microstructure evolution and mechanical properties of high-performance Al−Mn−Mg−Sc−Zr alloy fabricated by laser powder bed fusion

Hao TANG[1], Yao-xiang GENG[2], Chao-feng GAO[3], Xiao-ying XI[1], Jian-tao ZHANG[1], Zhi-yu XIAO[1]

1. National Engineering Research Center of Near-net Shape Forming for Metallic Materials, South China University of Technology, Guangzhou 510640, China;
2. School of Materials Science and Engineering, Jiangsu University of Science and Technology, Zhenjiang 212003, China;
3. Institute of Advanced Additive Manufacturing, Ji Hua Laboratory, Foshan 528200, China

Received 1 December 2022; accepted 21 June 2023

**Abstract:** The influence of aging temperatures on the microstructure and mechanical properties of an Al−Mn−Mg−Sc−Zr alloy prepared by laser powder bed fusion (L-PBF) was systematically studied. The results show that the fabricated alloy was a dense and crack-free piece with a fine grain size of 3.51 μm and a yield strength of (547±3) MPa. When the alloy was subjected to aging at 300 °C, a large amount of highly coherent $Al_3Sc$ nanoparticles (2−3 nm) precipitated from the Al matrix. The aged sample exhibited a high yield strength of (616±4) MPa, which can be attributed to precipitation strengthening, solid solution strengthening, and grain boundary strengthening. When the alloy was aged at a temperature higher than 300 °C, part of the dissolved Mn and Zr precipitated in the form of $Al_6Mn$ and $Al_3(Sc,Zr)$. When the alloy was aged at 500 °C, the $Al_6Mn$ and $Al_3(Sc,Zr)$ precipitates grew to approximately 600 and 30 nm, respectively, in size. Consequently, the yield strength of the alloy decreased to (372±3) MPa.

**Key words:** laser powder bed fusion; Al−Mn−Mg−Sc−Zr alloy; microstructure evolution; mechanical properties; $Al_3Sc$ nanoparticle

## 1 Introduction

Laser powder bed fusion (L-PBF) is an important laser additive manufacturing technique that can produce complex metal parts with high manufacturing flexibility [1]. Rapid solidification ($10^3$−$10^6$ K/s) nature of L-PBF technique can generate refined microstructure and increase the amount of solid elements in the prepared alloy. This, in turn, leads to mechanical properties that are comparable to, or even better than, those of traditional cast or wrought products [2,3]. Currently, a growing number of different materials can be manufactured by L-PBF, such as steels [4,5], titanium alloys [6,7], nickel alloys [8], aluminum alloys [2,9,10]. Among these, aluminum alloy is one of the most important materials owing to its high ductility, high specific strength and corrosion resistance [11,12]. Unfortunately, traditional high-strength wrought aluminum alloys, such as 2xxx and 7xxx alloys, exhibit poor hot-cracking resistance during the L-PBF process due to their wide freezing temperature range [13,14]. At present, majority of the commonly used L-PBF processed aluminum alloys are based on eutectic or near-eutectic Al−Si binary alloy because of their good castability and weldability [3]. However, their strength is inferior to that of high-strength wrought aluminum alloys [15].

**Corresponding author:** Zhi-yu XIAO, Tel/Fax: +86-20-87110099, E-mail: zhyxiao@scut.edu.cn
DOI: 10.1016/S1003-6326(24)66480-0

Recent researches on L-PBF processed aluminum alloys were focused on Sc- and Zr-modified Al−Mg and Al−Mn based alloys [16,17]. During L-PBF processing, primary $Al_3(Sc,Zr)$ precipitates formed during solidification. The presence of these precipitates can strengthen the $\alpha$(Al) grains and aid in mitigating hot-cracks. The high cooling rates of L-PBF processing greatly improved the solubility of alloying elements in the Al matrix, resulting in the formation of a supersaturated solid solution. Upon aging, this supersaturated matrix may precipitate a large amount of $Al_3Sc$ nanoparticles [18]. The low diffusion rate of Sc and the high coherence between $Al_3Sc$ and the $\alpha$(Al) matrix contributed to excellent thermal stability of the precipitates. This, along with the presence of solute elements like Mg, Mn, and Zr, effectively increased the strength of the alloy [19]. SCHMIDTKE et al [20] first reported the L-PBF processed crack-free Al−Mg−Sc−Zr alloy (Scalmalloy®, Al−4.5Mg−0.66Sc−0.37Zr). The mechanical properties were greatly improved after a simple post aging treatment of 4 h at 325 °C, with the ultimate tensile strength (UTS) and yield strength (YS) of the alloy reached at 530 and 520 MPa, respectively. SPIERINGS et al [16,21] systematically studied the microstructure evolution and strengthening mechanism of the L-PBF processed Sc- and Zr-modified Al−Mg alloy. JIA et al [22,23] developed a L-PBF processed Al−Mn−Sc aluminum alloy by introducing Mn into Al−Mg−Sc−Zr alloy to improve the effect of solid solution strengthening. This alloy demonstrated superior mechanical properties compared to Scalmalloy® with a YS of ~560 MPa. LI et al [24] designed a Si-containing Al−Mg−Sc−Zr alloy with a lower Sc content (0.5 wt.%), showing good L-PBF processability and mechanical properties. Recently, TANG et al [25,26] developed a novel L-PBF processed Al−Mn−Mg−Sc−Zr alloy with excellent mechanical property by increasing the contents of (Mn+Mg) and (Sc+Zr). This alloy exhibited an ultra-high YS of over 600 MPa at aging temperature of 300 °C.

The introduction of lattice defects (e.g. vacancies, dislocations and grain boundaries) through the L-PBF process has resulted in a decrease in the activation energy of $Al_3Sc$ and $Al_6Mn$ precipitates in the Al−Mn−Mg−Sc−Zr alloy. This has made the diffusion of Sc and Mn in the Al matrix easier than that was anticipated [22,27]. Therefore, investigating the evolution of microstructure and mechanical properties of L-PBF processed Al−Mn−Mg−Sc−Zr alloy at different aging temperatures may provide an important guide for the service limit of the alloy. In the present work, the influence of aging temperatures on microstructure and mechanical properties of a high-performance L-PBF processed Al−Mn−Mg−Sc−Zr alloy was systematically studied.

## 2 Experimental

### 2.1 Materials and L-PBF processing

Pre-alloyed Al−Mn−Mg−Sc−Zr powders with an average size of 38.81 μm were produced by vacuum induction gas atomization (VIGA). The chemical compositions of raw powders (Al−5.5Mn−2.7Mg−1.0Sc−0.9Zr) and printed sample (Al−5.2Mn−2.3Mg−1.0Sc−1.0Zr) were analyzed by an inductively coupled plasma emission spectrometer (ICP, PE OPTIMA 7300DV). L-PBF processed specimens with a size of 50 mm × 15 mm × 15 mm were fabricated using an EPM250 equipment via reciprocating scanning strategy, as shown in Fig. 1. The L-PBF processing parameters are listed in Table 1.

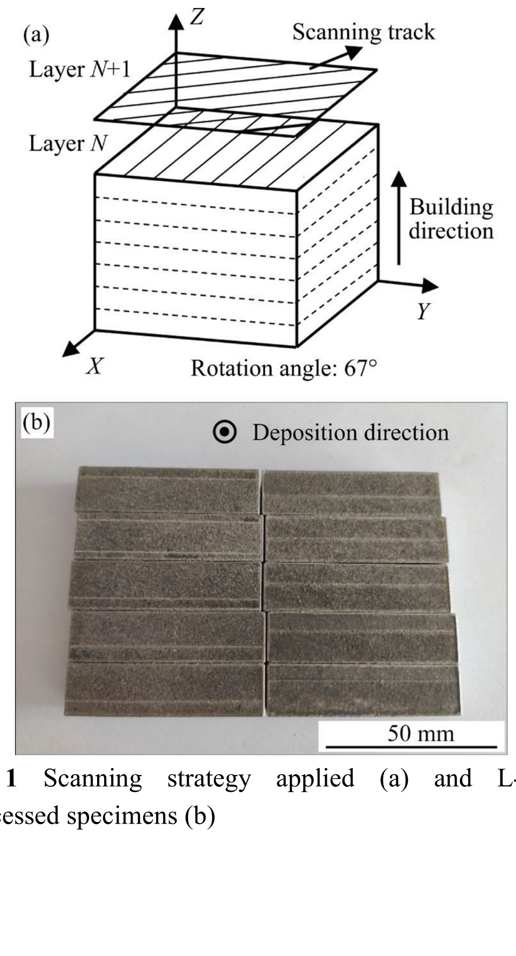


**Fig. 1** Scanning strategy applied (a) and L-PBF processed specimens (b)

**Table 1** L-PBF processing parameters

| Laser power/ W | Scanning speed/ (mm·s$^{-1}$) | Hatch spacing/μm | Beam radius/μm | Layer thickness/μm | Platform temperature/°C |
|---|---|---|---|---|---|
| 250, 350 | 800, 900, 1000, 1100, 1200 | 100 | 50 | 30 | 200 |

### 2.2 Materials characterization

Archimedes method was used to measure the real density of printed samples. The theoretical density, $\rho$, of the printed samples was calculated according to

$$\rho=\frac{1}{\sum(w_i/\rho_i)} \tag{1}$$

where $w_i$ is the mass faction of respective elements, and $\rho_i$ is the density of respective elements. Scanning electron microscope (SEM, JSM−6480, at 200 kV) was used to analyze the microstructure of the as-fabricated and aged samples. Before SEM observation, the samples were etched for 30 s using Keller's reagent (480 mL $H_2O$ + 10 mL $HNO_3$ + 6 mL HCL + 4 mL HF) in order to expose the microstructure of samples. The grain morphology of the alloy was analyzed using electron back scatter diffraction (EBSD), which was operated at 20 kV with a step size of 0.3 μm. EBSD samples were prepared by using electrolytic double spray thinning technique. The grain size was determined as the mean of the equivalent diameters of the grains based on the EBSD results. The transmission electron microscope (TEM) was a JEM−2010F with an accelerating voltage of 200 kV and high-resolution transmission electron microscopy (HRTEM) equipped with selected area electron diffraction (SAED) apparatus. The phase characterization was conducted by using X-ray diffraction (XRD, Bruker D8 Focus, Cu $K_\alpha$ radiation, $\lambda$=0.15406 nm). An Instron universal testing machine was used to study the tensile properties of the prepared samples at a constant strain rate of 1 mm/min according to ASTM7 E8—04. Each reported tensile data was the average of the results obtained from at least three different samples. The dimensions of tensile test samples are shown in Fig. 2. Vickers hardness measurements were performed on an HRS−150 microhardness tester with a load of 0.3 kg and a holding time of 15 s. The hardness tests were repeated seven times on each sample. A direct aging treatment was performed by holding the samples at 200, 300, 400, and 500 °C, respectively, for 2 h.

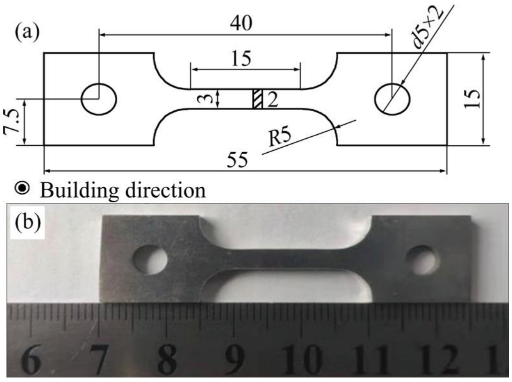


**Fig. 2** Schematic illustration (a) and photograph (b) of L-PBF processed tensile test specimen (unit: mm)

## 3 Results

### 3.1 Relative density

Laser volumetric energy density ($ED_V$) is an important parameter to evaluate the processability of L-PBF processed alloy. It is closely related to the melting degree of metal powder, dynamic behavior, and solidification characteristics of the molten pool, as well as defect formation during L-PBF process [28]. $ED_V$ is calculated according to $ED_V=P/v{\cdot}h{\cdot}t$ [29], where $P$ is laser power, $v$ is scanning speed, $h$ is hatching space, and $t$ is layer thickness. Figure 3 exhibits relative density of the L-PBF processed alloys as function of volumetric energy density. As depicted in Fig. 3, the relative density of samples exhibits a gradual increase with an increase in $ED_V$. It is observed that the samples fabricated at 350 W have a higher relative density. The maximum relative density of 99.8% can be achieved at an $ED_V$ of 145.8 J/mm$^3$. In this study, the threshold $ED_V$ for L-PBF processed alloy without key holes is about 80 J/mm$^3$, which is higher than the minimum energy input (60−70 J/mm$^3$) required for the complete melting of Al−Mg−Sc−Zr alloy powder that reported by SHI et al [30]. The reasons for this are, first, the present alloy contains more alloying elements, which may increase the melting temperature of the alloy. Second, different sizes of atoms increase the viscosity, which is not conducive to the spreading and wetting of the melt. Thus, higher $ED_V$ is required to achieve good processability of the present alloy [31].

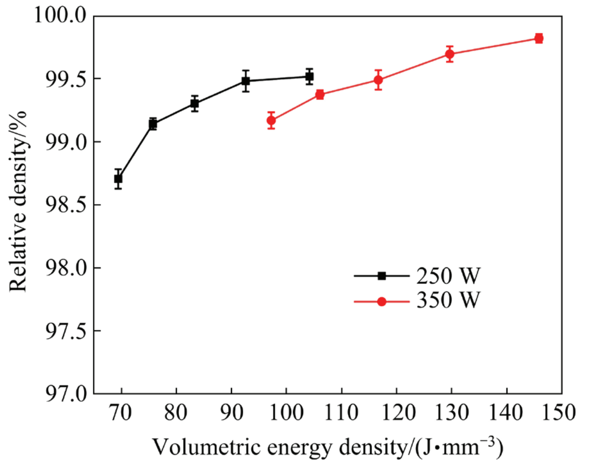


**Fig. 3** Relative density of L-PBF processed Al−Mn−Mg−Sc−Zr alloy at different laser powers as function of volumetric energy density

### 3.2 Microstructure

Figure 4 shows the EBSD orientation maps and $\alpha$(Al) grain size distribution of as-fabricated and aged at 500 °C for 2 h Al−Mn−Mg−Sc−Zr alloys. The as-fabricated alloy reveals a duplex grain structure with fine equiaxed grains located at the boundary of molten pool and columnar grains at the center of molten pool. These grains have an average grain size of about 3.51 μm, which is similar to that of other Sc-modified aluminum alloys produced by L-PBF process [22]. After undergoing aging treatment at 500 °C for 2 h, this alloy retains its columnar-equiaxed bimodal microstructure with an average grain size of approximately 4.16 μm. The absence of noticeable grain coarsening suggests that the $\alpha$(Al) grain exhibits exceptional thermal stability.

Figure 5 shows XRD patterns of the L-PBF processed Al−Mn−Mg−Sc−Zr alloy after aging treatment at different temperatures for 2 h. The $\alpha$(Al) and $Al_6Mn$ phases are detected in all samples. The samples are likely to include $L1_2$ type phase, which highly agrees with the findings of Refs. [22,26]. With the increase in aging temperature, the position of the major $\alpha$(Al) diffraction peak ($2\theta$) first shifts

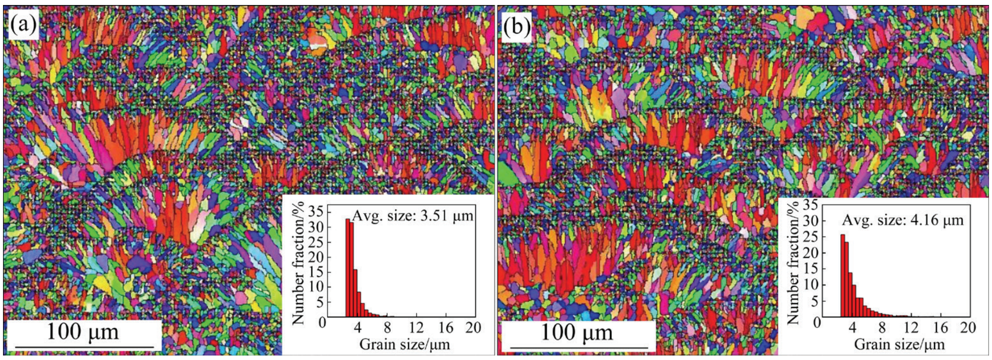


**Fig. 4** EBSD orientation maps of $\alpha$(Al) grains in L-PBF processed Al−Mn−Mg−Sc−Zr alloy: (a) As-fabricated; (b) Aged at 500 °C for 2 h (Insets are the grain size distribution maps)

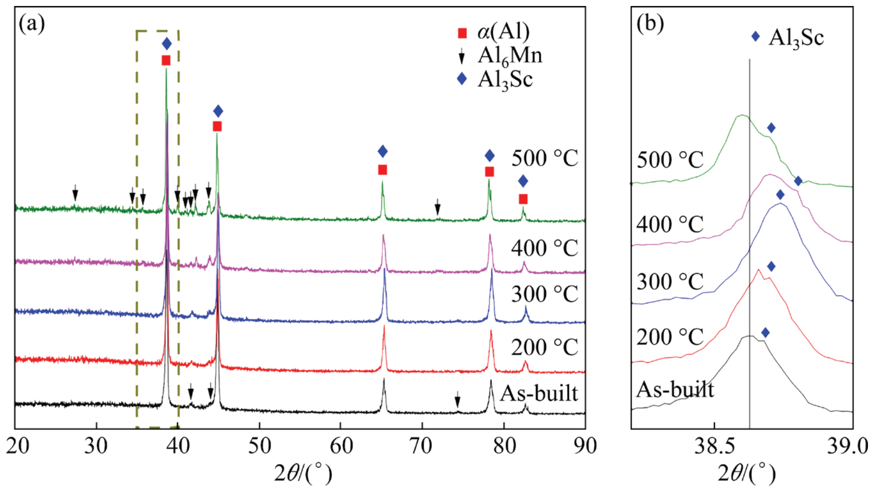


**Fig. 5** XRD patterns of L-PBF processed Al−Mn−Mg−Sc−Zr alloy aged at different temperatures for 2 h (a) and local enlargement of XRD patterns (b)

to high angle and then to low angle, as shown in Fig. 5(b). When the aging temperature is over 300 °C, the intensity of $Al_6Mn$ diffraction peaks increases and the width of diffraction peaks decreases obviously (Fig. 5(a)), indicating that the volume fraction and the grain size of $Al_6Mn$ increase [29]. When samples are aging-treated at 200 and 300 °C, respectively, the concentration of large-radius Sc in $\alpha$(Al) solid solution is reduced due to the precipitation of $Al_3Sc$ nanoparticles, resulting in the $\alpha$(Al) diffraction peaks shifting to higher angle [26,30]. As the aging temperature increases to 400 and 500 °C, respectively, the precipitation and growth of $Al_6Mn$ phase lead to the reduction of dissolved Mn element in $\alpha$(Al) matrix and make the diffraction peaks of $\alpha$(Al) move to lower angle [31,32].

TEM bright field images show that the microstructure of the as-fabricated Al−Mn−Mg−Sc−Zr sample contains fine and coarse grains with a large number of nanoparticles embedded in the grain boundaries (Figs. 6(a) and (b)). According to our previous report [26], the fine grain boundaries mainly contain $Al_6Mn$ and $Al_3$(Sc,Zr) particles, and only $Al_6Mn$ particles are embedded in coarse grain boundaries. Besides, $Al_3Sc$ and $Al_6Mn$ particles are identified by HRTEM image and the corresponding inverse fast Fourier transforms (IFFT) patterns, as shown in Fig. 6(c). Figure 6(d) shows a primary $Al_3$(Sc,Zr) particle embedded in equiaxed grain boundary with a diameter of around 80 nm, which is identified by measuring the crystal plane spacing in Fig. 6(e). According to the fast Fourier transform (FFT) pattern analysis, the primary $Al_3$(Sc,Zr) shows

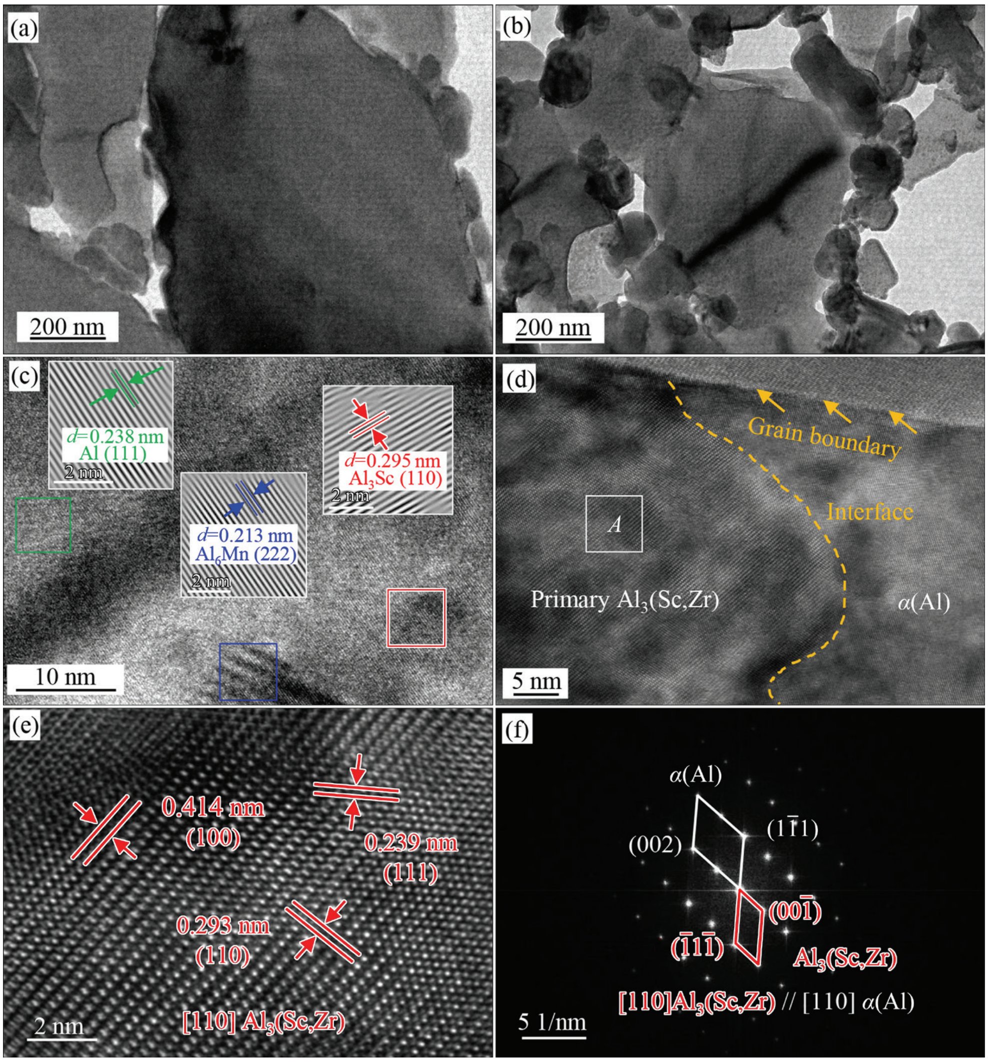


**Fig. 6** TEM bright-filed images of as-fabricated sample obtained from columnar grain (a) and equiaxed grain (b), HRTEM image and corresponding IFFT patterns (inset) of equiaxed grain (c), HRTEM (d) and amplified HRTEM image (e) of Zone *A* in (d), and corresponding FFT pattern of coherent primary $Al_3$(Sc,Zr) (f)

a fully coherent orientation relationship with the $\alpha$(Al) matrix, which indicates that it can serve as the nucleation site for $\alpha$(Al) during the solidification [23,26].

Figure 7 shows TEM images of L-PBF processed Al−Mn−Mg−Sc−Zr alloy aged at 300 °C for 2 h. In Figs. 7(a, $b_1$, $b_2$), an enlarged TEM image confirms that nano-clusters of Sc do not contain Zr element. In Fig. 7(d), the HRTEM image and IFFT pattern reveal that a large amount of nano-sized $Al_3Sc$ particles, with a size of 2−3 nm, precipitated from $\alpha$(Al) matrix. Moreover, these nano-sized $Al_3Sc$ particles have the $L1_2$ structure and keep a good coherency with Al matrix (Fig. 7(e)) [33].

In Fig. 8, the EDS mappings reveal that both Mn-rich phase and (Sc,Zr)-rich phase are presented in the sample aged at 500 °C, and these two phases correspond to primary $Al_6Mn$ and secondary $Al_3$(Sc,Zr) precipitates [34,35]. This finding is consistent with the SAED results (Figs. 9(b, f)). Apparently, the size of primary $Al_6Mn$ reaches 600 nm and secondary $Al_3$(Sc,Zr) also coarsens to a size of 30−100 nm. The diameter of secondary $Al_3$(Sc,Zr) particles is much larger than that of $Al_3Sc$ nanoparticles (2−3 nm). It is likely caused by the faster diffusion rate of alloying elements at an elevated aging temperature [36]. Figure 9(c) shows several secondary $Al_6Mn$ grains with coarsened needle shape. Figure 9(d) reveals a special 7R structure, which was identified by the HRTEM image and corresponding FFT pattern (Fig. 9(e)). According to LI et al [24], it can distort the lattice at the interfaces and act as a strong barrier to keep dislocations away from moving freely. HRTEM image and FFT pattern (Fig. 9(f)) of the sample aged at 500 °C demonstrate that the coarsened secondary $Al_3$(Sc,Zr) particles still maintain a high level of coherency with Al matrix.

### 3.3 Mechanical properties

Figure 10(a) shows the Vickers hardness of L-PBF processed Al−Mn−Mg−Sc−Zr alloys. The hardness of as-fabricated sample remains constant at around HV 180, indicating that scanning speed and laser power have no obvious influence on the sample hardness. The sample hardness after aging treatment at different temperatures for 2 h is presented in Fig. 10(b). The Vickers hardness of the samples exhibits a non-linear trend, initially increasing and subsequently decreasing with an increase in aging temperature, which corresponds to the under-aging, peak-aging and over-aging stages. The sample hardness reaches a maximum of HV (219±2) at the peak-aging temperature of 300 °C while significantly decreases to HV (148±1) at 500 °C.

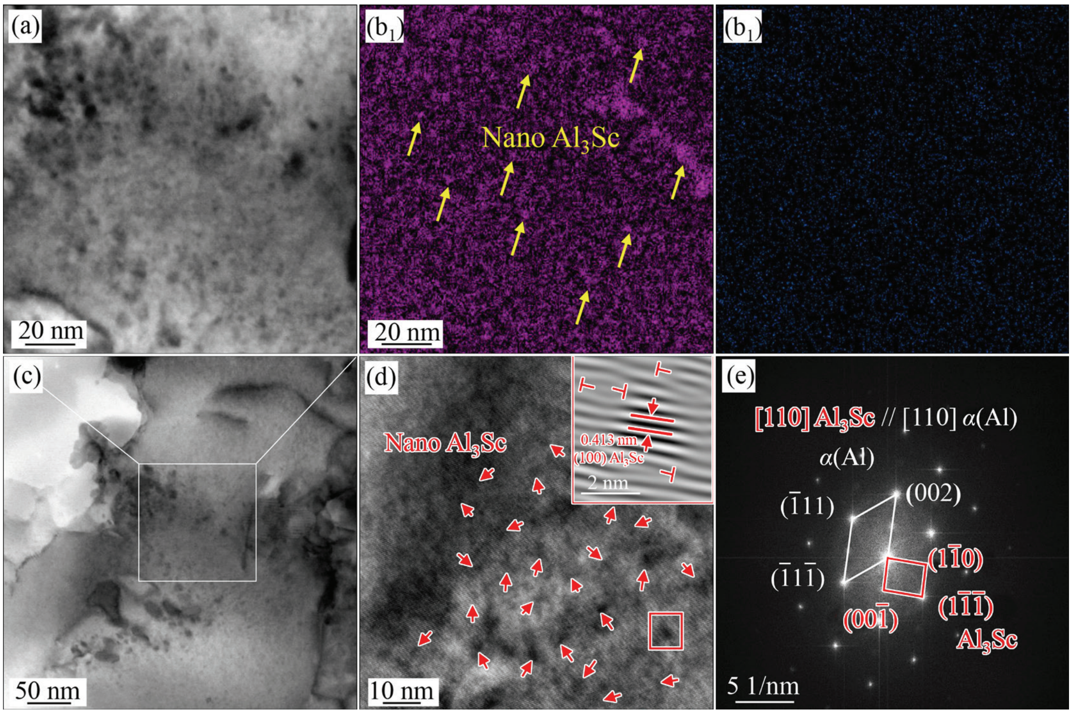


**Fig. 7** TEM image of L-PBF processed Al−Mn−Mg−Sc−Zr alloy aged at 300 °C for 2 h (a) and TEM bright-field image (c), EDS mappings of Sc ($b_1$) and Zr ($b_2$) elements, HRTEM image (d) and corresponding FFT pattern (e)

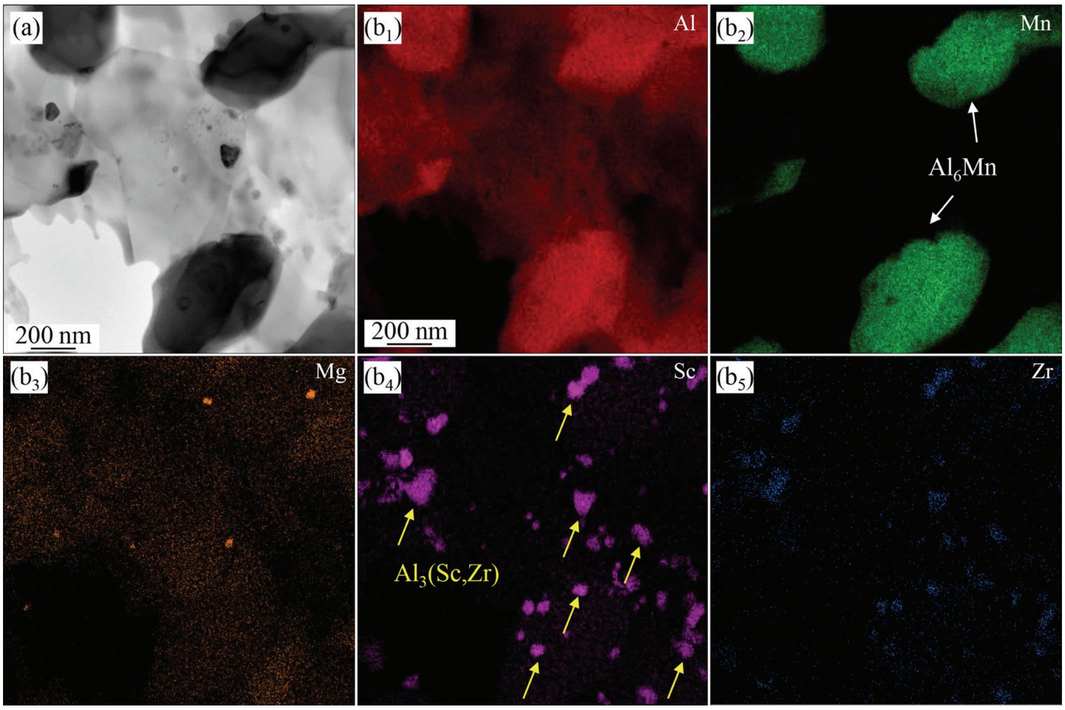


**Fig. 8** TEM image (a) and EDS mappings of main elements ($b_1$−$b_5$) in L-PBF processed Al−Mn−Mg−Sc−Zr alloy aged at 500 °C for 2 h

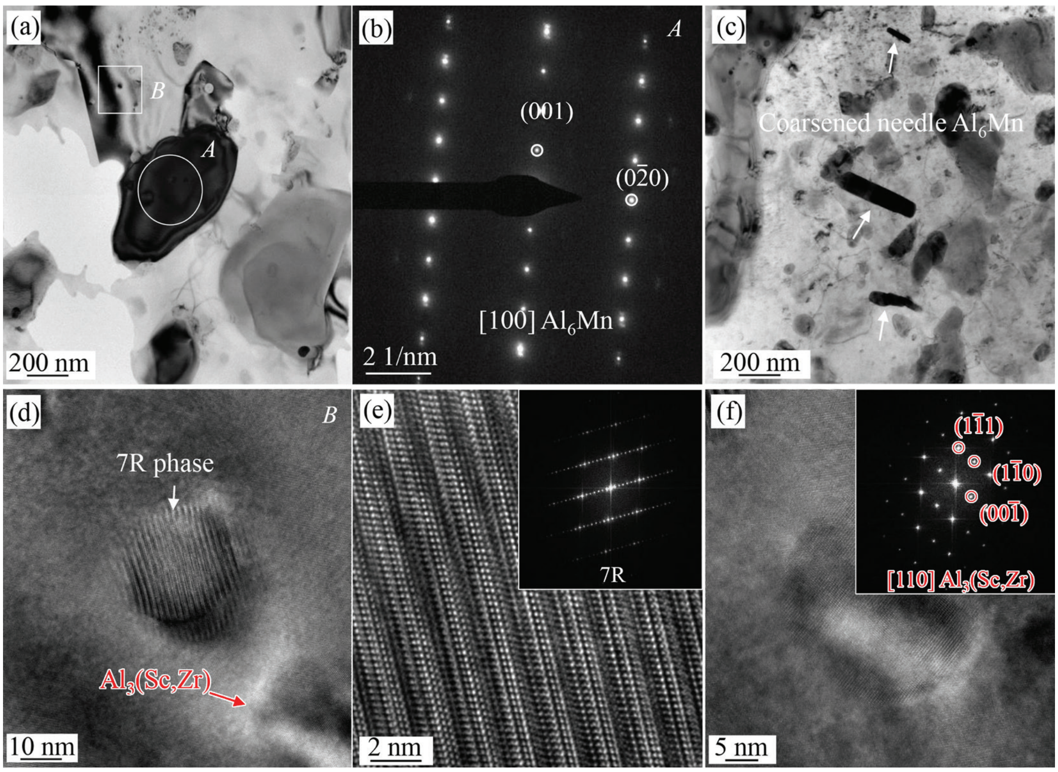


**Fig. 9** TEM image of L-PBF processed Al−Mn−Mg−Sc−Zr alloy aged at 500 °C for 2 h (a) and TEM bright-field image (c), corresponding SEAD pattern (b) of Zone *A* in (a), HRTEM image (d) of Zone *B* in (a), amplified HRTEM image of 7R phase (e), and HRTEM image and FFT pattern of secondary $Al_3(Sc,Zr)$ (f)

Tensile tests were performed on as-fabricated and aged samples to further reveal the influence of aging temperature on the mechanical properties of L-PBF processed Al−Mn−Mg−Sc−Zr alloys. Tensile stress−strain curves are shown in Fig. 11(a). The tensile curve of sample aged at 500 °C for 2 h

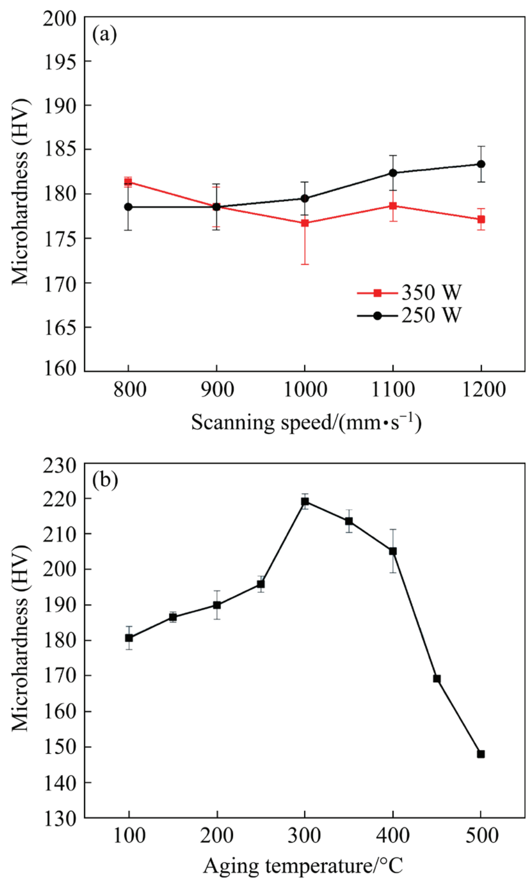


**Fig. 10** Evolution of Vickers hardness of as-fabricated Al−Mn−Mg−Sc−Zr alloy (a) and samples after aging treatment at different temperatures for 2 h (b)

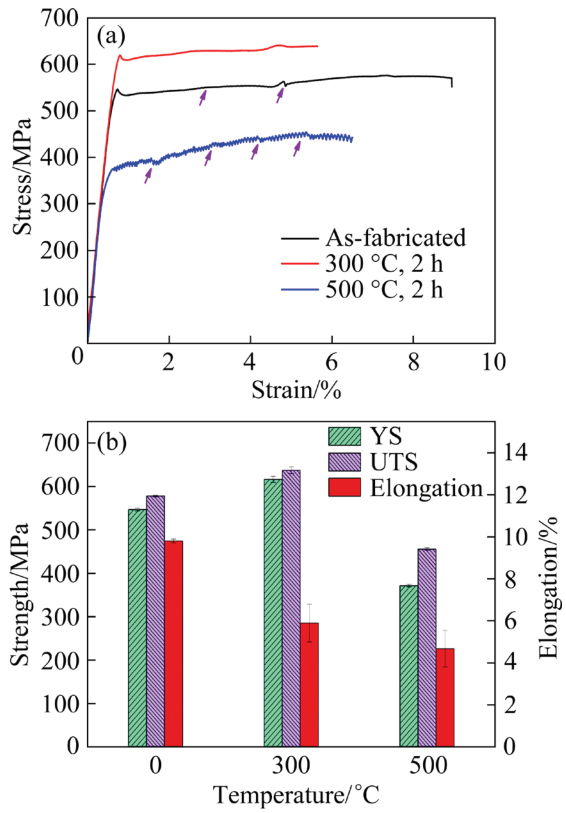


**Fig. 11** Tensile stress−strain curves (a) and tensile properties (b) of as-fabricated samples and samples after aging treatment at different temperatures for 2 h

displays serrations, as evidenced by the visible purple markings on its curve. The serrations are related to the Portevin-Le-Chatelier (PLC) effect typically in Al−Mg alloys [37]. The UTS, YS and elongation of as-fabricated samples are (578±2) MPa, (547±3) MPa, and (9.8±0.1)%, respectively (see Fig. 11(b)). After being subjected to an aging temperature of 300 °C, a notable improvement in tensile strength can be observed. The UTS and YS reached a maximum of (637±8) and (616±4) MPa, respectively. However, this is accompanied by a reduction in elongation, which decreases to (5.9±0.9)%. The YS value is superior to that of most of the previously reported wrought 7075 aluminum alloy [38]. Nevertheless, the material's tensile properties experience a significant decline when the aging temperature is raised to 500 °C. The recorded values for UTS, YS, and elongation are (456±3) MPa, (372±3) MPa, and (4.7±0.9)%, respectively. These results suggest that the material is no longer thermally stable after being aged at this temperature.

## 4 Discussion

### 4.1 Microstructure evolution

Aging treatment can affect the microstructure of the alloy by stimulating the precipitation of nanoparticles and the coarsening of particles and grains [19]. Schematic diagrams of the microstructure evolution of the L-PBF processed Al−Mn−Mg−Sc−Zr alloy at different heat treatment temperatures are illustrated in Fig. 12. During solidification, primary $Al_3(Sc,Zr)$ particles will first form in the melt. They may serve as nucleation sites for $\alpha$(Al) grains, exhibiting a strong grain refining effect. The formation of fine grains upon solidification is the main reason for the absence of cracks in the L-PBF processed Al−Mn−Mg−Sc−Zr alloy [24]. An increase in the velocity of the solidification front can result in solute trapping, which in turn hinders the formation of the primary $Al_3(Sc,Zr)$ particles. Meanwhile, the residual melt tends to form columnar grains that grow predominantly along the [100] direction during solidification [23,39,40]. At the same time, the redundant Mn elements in $\alpha$(Al)

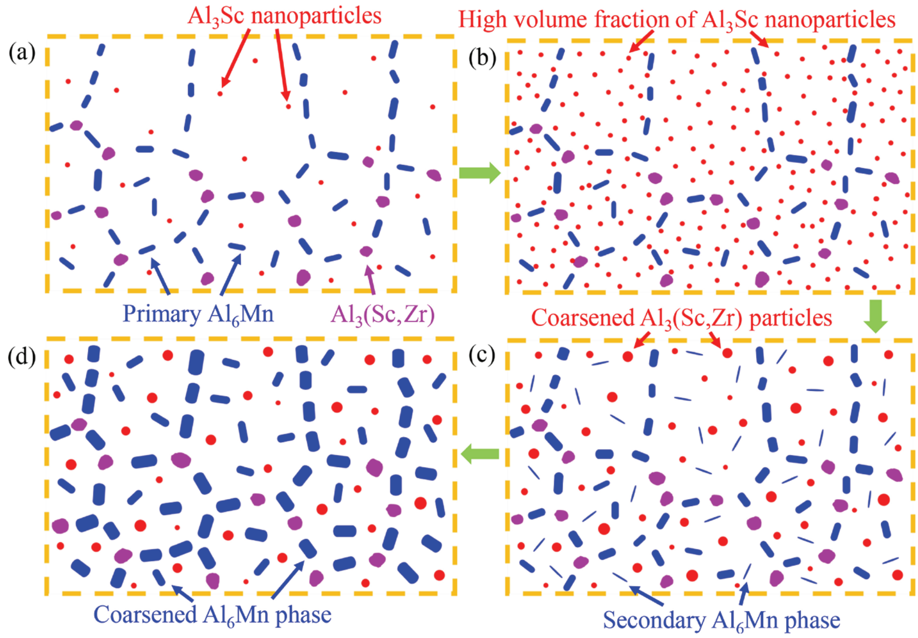


**Fig. 12** Schematic diagrams of microstructural evolution of L-PBF processed Al−Mn−Mg−Sc−Zr alloy at different aging temperatures: (a) As-fabricated; (b) Aged at 300 °C for 2 h; (c) Aged at 400 °C for 2 h; (d) Aged at 500 °C for 2 h

are discharged from the grain, forming $Al_6Mn$ nanoparticles at both of the equiaxed and columnar grain boundaries (Fig. 12(a)). During the L-PBF process, an intrinsic heat treatment effect will be introduced by the layer-by-layer material deposition, which will induce the precipitation of $Al_3Sc$ and $Al_6Mn$ from equiaxed grains, as shown in Fig. 12(a). The sample aged at 300 °C shows a high number density of coherent fine $Al_3Sc$ nanoparticles precipitated from the $\alpha$(Al) matrix due to the high diffusivity of Sc in aluminum alloy (Figs. 7(d) and 12(b)) [41]. JIA et al [22] utilized a three-dimensional atomic probe to confirm the presence of Sc-rich clusters in the as-fabricated Al−Mn−Sc alloy. These clusters were found to be a result of intrinsic heat treatment during the L-PBF process. The Sc-rich clusters can serve as precursors for precipitate growth, resulting in a considerable decrease in the energy required for the growth of $Al_3Sc$ precipitates in comparison to traditional Al−Sc alloy [22,42]. At this temperature, the Mn-related precipitation (i.e., $Al_6Mn$) is not activated. When the aging temperature increases to 400 °C, a large number of needle-shaped secondary $Al_6Mn$ particles precipitate from the $\alpha$(Al) matrix (Fig. 12(c)). The higher activation energy for the lattice diffusion of Mn in Al compared to Sc in Al results in a higher precipitation temperature of $Al_6Mn$ [42]. At this aging temperature (400 °C), the primary $Al_6Mn$ precipitates embedded in the grain boundaries grow rapidly (Fig. 12(c)). On the one hand, high cooling rate of the L-PBF technique increases the concentration of dissolved Mn and Zr elements in the $\alpha$(Al) solid solution. This results in rapid segregation of Mn, which is helpful for the nucleation and growth of precipitates. Meanwhile, the rapid diffusion of Zr at high temperature may facilitate the segregation of Zr towards $Al_3Sc$ nanoparticles. On the other hand, the L-PBF process generates a high-density of dislocations and a large fraction of grain boundaries, which can serve as fast diffusion channels to promote the rapid diffusion of elements and the growth of $Al_6Mn$ and $Al_3(Sc,Zr)$ during the aging process [22]. At 500 °C, the size of precipitates further increases, as shown in Fig. 12(d). The grain size of the samples remains relatively constant after being aged at different temperatures for 2 h. This may be attributed to the presence of $Al_3(Sc,Zr)$ and $Al_6Mn$ precipitates, which are located at the grain boundaries and act as effective inhibitors against recrystallization and grain growth [22,23].

### 4.2 Strengthening mechanisms

The high tensile performance of Al−Mn−Mg−Sc−Zr alloys processed through L-PBF and aged at 300 °C for 2 h, exhibiting a yield strength of (616±4) MPa, can be attributed to three primary strengthening mechanisms, namely, solid solution strengthening, precipitation strengthening, and grain boundary strengthening.

4.2.1 Solid solution strengthening

The L-PBF process results in an ultrahigh cooling rate, which allows the alloying elements Mn, Mg, Sc, and Zr to become supersaturated in $\alpha$(Al). This high solute content leads to solid solution strengthening. Localized strain fields can be generated by the mismatch in atomic size and the shear modulus of alloying elements in the solid solution matrix. The interaction of localized strain fields can greatly enhance the tensile properties of materials by hindering the movement of dislocations [43]. According to Ref. [44], the contribution of solid solution strengthening to the yield strength increment is given by

$$\Delta\sigma_{ss}=M\left(\frac{3}{8}\right)^{2/3}\left(\frac{1+\nu}{1-\nu}\right)^{4/3}\left(\frac{w}{b}\right)^{1/3}G\,|\varepsilon|^{4/3}c^{2/3} \quad (2)$$

where $M$ is the average Taylor factor (3.06 for Al); $\nu$ is the Poisson ratio (0.345 for Al); $w$(=5$b$), $b$ is the amplitude of the Burgers vector of Al ($b$=0.286 nm); $G$(=25.4 GPa) is the shear modulus of Al; $\varepsilon$ is the lattice misfit strain between Al and solid solution atoms (4.40% for Mn, 1.28% for Mg, and 1.35% for Zr) [44,45]; $c$ refers to the molar fraction of solute elements in the Al matrix. According to EDS measurements, the contents of Mn, Mg, and Zr in Al matrix are around 1.53 at.%, 1.26 at.%, and 0.18 at.%, respectively. The total contribution of solid solution strengthening can be calculated to be ~210.5 MPa.

4.2.2 Precipitation strengthening

The precipitation strengthening is primarily due to the precipitation of high volume fraction of $Al_3Sc$ nanoparticles. Upon subjecting the sample to a temperature of 300 °C, a significant amount of fully coherent $Al_3Sc$ particles with a nano-size of approximately 2 nm precipitated from the matrix were observed (Figs. 7(a, d, e)). $Al_3Sc$ nanoparticles can effectively pin and imped the movement of dislocations due to the substantial difference in modulus between the secondary phase and surrounding Al matrix. The entangled dislocation within Al grains can be observed in Fig. 13(a). The interaction between the $Al_3Sc$ nanoparticles and dislocation, and an obvious pinning effect are presented in Fig. 13(b). Therefore, the mechanical properties of the Al−Mn−Mg−Sc−Zr alloy are improved due to the precipitation the strengthening caused by secondary $Al_3Sc$ nanoparticles precipitated during aging treatment [45]. However, the dislocation loops in Fig. 13(b) demonstrate that both shearing mechanism and Orowan bypassing mechanism exist in that specimen. Previous study [44] proved that the transition from shearing mechanism to Orowan dislocation looping mechanism occurs for the $Al_3Sc$ particles with size over 2.1 nm. Therefore, the precipitation strengthening in the present prepared alloy is dominated by shearing mechanism. The precipitation strengthening can be estimated from modulus strengthening ($\Delta\sigma_{modulus}$) according to Eq. (3) [25]:

$$\Delta\sigma_{modulus}=0.0055M(\Delta G)^{3/2}\left(\frac{2f_v}{G}\right)^{1/2}\left(\frac{R}{b}\right)^{\left(\frac{3m}{2}-1\right)} \quad (3)$$

where $\Delta G$(=42.6 GPa) is the difference in modulus between $Al_3Sc$ and Al matrix; $f_v$ is the volume fraction of $Al_3Sc$ nanoparticles (~1.73%) calculated from Fig. 7(d); $R$ is the mean radius (1.5 nm) of $Al_3Sc$ nanoparticles; $m$(=0.85) is a constant. Thus, the contribution of $Al_3Sc$ nanoparticles to the yield strength increment is ~272.4 MPa.

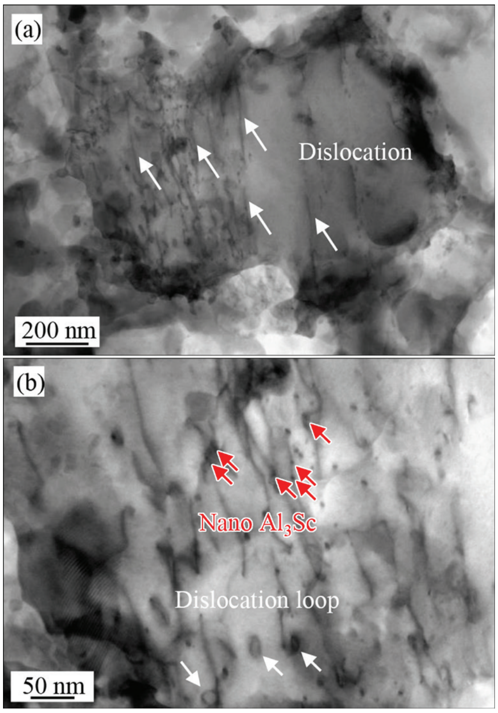


**Fig. 13** TEM bright-field images showing high volume fraction of dislocations inside grain (a), and dislocations interacting with intragranular $Al_3Sc$ nanoparticles (b)

4.2.3 Grain boundary strengthening

The exceptional mechanical properties of the L-PBF processed Al−Mn−Mg−Sc−Zr alloy can also be associated with its ultra-fine grain microstructure. L-PBF generates a significant grain refinement effect through super cooling [46]. The precipitation of primary $Al_3(Sc,Zr)$ phases also increases the potential nucleation sites and refines $\alpha$(Al) grains efficiently. According to Hall−Petch relationship applied in the strength of polycrystalline metals [47], the finer the grains (Fig. 4(a)) are, the more the grain boundaries are, and the more pronounced the grain boundary strengthening is. The primary phases of $Al_3(Sc,Zr)$ and $Al_6Mn$ are distributed along the grain boundaries, which can prevent grain boundary movement through the Zener pinning effect. These phases also act as effective inhibitors of grain growth during aging treatment [48]. The samples can maintain a very fine microstructure even after being aged at 500 °C for 2 h. The high thermal stability of the current alloy is primarily due to the presence of thermally stable nanoparticles of $Al_3Sc$ and $Al_6Mn$. These nanoparticles act as strong inhibitors of grain growth, preventing any unwanted increase in grain size [22,28]. The yield strength change resulting from grain boundary strengthening for samples aged at 300 °C for 2 h can be calculated by

$$\Delta\sigma_{GB}=\sigma_0+kd^{-1/2} \tag{4}$$

where $\sigma_0$(=20 MPa) is the resistance of Al lattice to dislocation motion; $k$ is the Hall−Petch coefficient set as 0.17 MPa·m$^{1/2}$; $d$ (~3.8 μm) is the average grain size measured from TEM results. Therefore, the contribution of grain boundary strengthening can be calculated to be ~107.2 MPa. Based on above analysis, the total yield strength ($\sigma_Y$) can be estimated as

$$\sigma_Y=\Delta\sigma_{GB}+\Delta\sigma_{SS}+\Delta\sigma_{modulus} \tag{5}$$

The calculated $\sigma_Y$ is equal to ~590.1 MPa, which is slightly lower than the measured yield strength ((616±4) MPa). The unaccounted strength increment is considered to come from the primary $Al_3(Sc,Zr)$, 7R phase, and $Al_6Mn$ phase [24].

When the aging temperature is increased to 500 °C, both Vickers hardness and tensile properties decrease dramatically and are even inferior to those of the as-fabricated samples (Figs. 10(b) and 11(b)). As shown in EBSD results (Figs. 4(b, d)), the grains exhibit slight growth, which in turn lead to a reduction in grain boundary strengthening. The XRD results confirm that some of the Mn dissolved in the Al solid solution is precipitated, forming secondary $Al_6Mn$. Additionally, the diffusion rates of Sc and Zr increase at higher temperature, causing the gradual growth of primary $Al_3(Sc,Zr)$ and secondary $Al_3Sc$ particles. This results in the loss of pinning effect [22,49]. Overall, the precipitation strengthening from $Al_3Sc$ particles and the solid solution strengthening of Mn, Sc, and Zr in $\alpha$(Al) lose their effectiveness. As a result, the sample aged at 500 °C exhibits a decrease in hardness and tensile strength.

An obvious PLC effect can be observed in the stress−strain curve of the sample aged at 500 °C (Fig. 11(a)). Based on the reported researches [50,51], this may be associated with the reasons as follows: the release of mobile and immobile dislocations primarily occurred near the solute atoms; additionally, secondary particles precipitate along and pin around these dislocations. Hence, the movement of dislocations is hindered and slightly higher stress is required to tear them off in the plastic deformation [17]. Once the dislocation crossed the hindrance of the solute atoms and secondary particles, a rapid stress drop occurred until the dislocation was blocked again, thereby forming the observed serrations in the stress−strain curves.

## 5 Conclusions

(1) The tested alloy has good processability. The density of L-PBF processed Al−Mn−Mg−Sc−Zr alloy can be enhanced by using a higher laser energy density. Near fully dense sample with a relative density of 99.8% can be obtained by using an $ED_V$ of 145.8 J/mm$^3$ with the help of a preheated substrate.

(2) The microstructure of the L-PBF processed Al−Mn−Mg−Sc−Zr alloy exhibits an equiaxed-columnar grain structure with an average grain size of 3.51 μm. The primary $Al_6Mn$ distributes at both fine grain and coarse grain boundaries; however, $Al_3(Sc,Zr)$ particles only are embedded in fine grain boundaries. An UTS of (578±2) MPa and a YS of (547±3) MPa with an elongation of (9.8±0.1)% are achieved in the as-fabricated samples.

(3) Typical under-aging, peak-aging and over-aging stages can be observed in the designed aging

experiments. At the peak-aging temperature of 300 °C, a large number density of highly coherent $Al_3Sc$ nanoparticles (2−3 nm) precipitated from the Al matrix. As a result, the maximum UTS of (637±8) MPa and YS of (616±4) MPa with elongation of (5.9±0.9)% were obtained. The high mechanical property is mainly attributed to the fine microstructure, the high solute content, and the precipitation of a large amount of coherent $Al_3Sc$ particles.

(4) When the aging temperature reaches 500 °C, over-aging happened and the UTS and YS decreased to (456±3) MPa and (372±3) MPa, respectively. The particle sizes of the $Al_6Mn$ and $Al_3(Sc,Zr)$ precipitates in the sample aged at 500 °C for 2 h coarsened to approximately 600 and 30 nm, respectively, indicating that the alloy was no longer thermally stable at high temperatures. The reduction in strength was primarily caused by the growth of grains, coarsening of secondary $Al_3Sc$ and $Al_6Mn$ particles, and the dissolution of Mn, Sc, and Zr in the solid solution matrix.

## CRediT authorship contribution statement

**Hao TANG:** Conceptualization, Methodology, Investigation, Writing − Original draft; **Yao-xiang GENG:** Resources, Methodology, Review & editing, Supervision; **Chao-feng GAO:** Methodology, Funding, Review & editing, Supervision; **Xiao-ying XI:** Conceptualization, Review & editing; **Jiao-tao ZHANG:** Funding, Review & editing, Supervision; **Zhi-yu XIAO:** Resources, Funding, Review & editing, Supervision, Project administration.

## Declaration of competing interest

The authors declare that they have no known competing financial interests or personal relationships that could have appeared to influence the work reported in this paper.

## Acknowledgments

The authors are grateful for the financial supports from the National Natural Science Foundation of China (Nos. 52001140, 52274363), and the Guangdong Basic Applied Basic Research Foundation, China (Nos. 2022A1515010558, 2022A1515011597, 2022A1515240065)

## References

[1] CAO Y, LIN X, WANG Q Z, SHI S Q, MA L, KANG N, HUANG W D. Microstructure evolution and mechanical properties at high temperature of selective laser melted $AlSi_{10}Mg$ [J]. Journal of Materials Science & Technology, 2021, 62: 162−172.

[2] BAYOUMY D, SCHLIEPHAKE D, DIETRICH S, WU X H, ZHU Y M, HUANG A J. Intensive processing optimization for achieving strong and ductile Al−Mn−Mg−Sc−Zr alloy produced by selective laser melting [J]. Materials & Design, 2021, 198: 109317.

[3] WANG Pei, ECKERT J, PRASHANTH K G, WU Ming-wei, KABAN I, XI Li-xia, SCUDINO S. A review of particulate-reinforced aluminum matrix composites fabricated by selective laser melting [J]. Transactions of Nonferrous Metals Society of China, 2020, 30: 2001−2034.

[4] LIU Jue, DONG Shi-yun, JIN Xin, WU Peng-yue, YAN Shi-xing, LIU Xiao-ting, TAN Yong-hao. Quality control of large-sized alloy steel parts fabricated by multi-laser selective laser melting (ML-SLM) [J]. Materials & Design, 2022, 223: 111209.

[5] ZHANG Jian-tao, ZHU Yuan-zhi, XI Xiao-ying, XIAO Zhi-yu. Altered microstructure characteristics and enhanced corrosion resistance of UNS S32750 duplex stainless steel via ultrasonic surface rolling process [J]. Journal of Materials Processing Technology, 2022, 309: 117750.

[6] BARTOLOMEU F, BUCIUMEANU M, PINTO E, ALVES N, SILVA F S, CARVALHO O, MIRANDA G. Wear behavior of $Ti_6Al_4V$ biomedical alloys processed by selective laser melting, hot pressing and conventional casting [J]. Transactions of Nonferrous Metals Society of China, 2017, 27: 829−838.

[7] COSTA M M, DANTAS T A, BARTOLOMEU F, ALVES N, SILVA F S, MIRANDA G, TOPTAN F. Corrosion behaviour of PEEK or $\beta$-TCP-impregnated $Ti_6Al_4V$ SLM structures targeting biomedical applications [J]. Transactions of Nonferrous Metals Society of China, 2019, 29: 2523−2533.

[8] YUE Tian-yang, ZHANG Sheng, WANG Chao-yue, XU Wei, XU Yi-di, SHI Yu-sheng, ZANG Yong. Effects of selective laser melting parameters on surface quality and densification behaviours of pure nickel [J]. Transactions of Nonferrous Metals Society of China, 2022, 32: 2634−2647.

[9] QI J F, LIU C Y, CHEN Z W, LIU Z Y, TIAN J S, FENG J, OKULOV I V, ECKERT J, WANG P. Enhancement in strength and thermal stability of selective laser melted Al−12Si by introducing titanium nanoparticles[J]. Materials Science and Engineering A, 2022, 855: 143833.

[10] GENG Yao-xiang, TANG Hao, XU Jun-hua, HOU Yu, WANG Yu-xin, HE Zhen, ZHANG Zhi-jie, JU Hong-bo, YU Li-hua. Influence of process parameters and aging treatment on the microstructure and mechanical properties of $AlSi_8Mg_3$ alloy fabricated by selective laser melting [J]. International Journal of Minerals, Metallurgy and Materials, 2022, 29: 1770−1779.

[11] ZHANG Jin-liang, SONG Bo, WEI Qing-song, BOURELL D, SHI Yu-sheng. A review of selective laser melting of aluminum alloys: Processing, microstructure, property and developing trends [J]. Journal of Materials Science & Technology, 2019, 35: 270−284.

[12] ZHANG Han, GU Dong-dong, YANG Jian-kai, DAI Dong-hua, ZHAO Tong, HONG Chen, GASSER A, POPRAWE R. Selective laser melting of rare earth element Sc modified aluminum alloy: Thermodynamics of precipitation behavior and its influence on mechanical properties [J]. Additive Manufacturing, 2018, 23: 1−12.

[13] ZHANG Hu, ZHU Hai-hong, QI Ting, HU Zhi-heng, ZENG Xiao-yan. Selective laser melting of high strength Al−Cu−Mg alloys: Processing, microstructure and mechanical properties [J]. Materials Science and Engineering A, 2016, 656: 47−54.

[14] WANG Zi-hong, LIN Xin, KANG Nan, CHEN Jing, TAN Hua, FENG Zhe, QIN Ze-hao, YANG Hai-ou, HUANG Wei-dong. Laser powder bed fusion of high-strength Sc/Zr-modified Al−Mg alloy: phase selection, microstructural/ mechanical heterogeneity, and tensile deformation behavior [J]. Journal of Materials Science & Technology, 2021, 95: 40−56.

[15] LI X P, JI G, CHEN Z, ADDAD A, WU Y, WANG H W, VLEUGELS J, HUMBEECK J V, KRUTH J P. Selective laser melting of nano-$TiB_2$ decorated $AlSi_{10}Mg$ alloy with high fracture strength and ductility [J]. Acta Materialia, 2017, 129: 183−193.

[16] SPIERINGS A B, DAWSON K, VOEGTLIN M, PALM F, UGGOWITIZER P J. Microstructure and mechanical properties of as-processed scandium-modified aluminium using selective laser melting [J]. CIRP Annals, 2016, 65: 213−216.

[17] LI Rui-di, CHEN Hui, ZHU Hong-bin, WANG Min-bo, CHEN Chao, YUAN Tie-chui. Effect of aging treatment on the microstructure and mechanical properties of Al−3.02Mg−0.2Sc−0.1Zr alloy printed by selective laser melting [J]. Materials & Design, 2019, 168: 107668.

[18] GRIFFITHS S, CROTEAU J R, ROSSELL M D, ERNI R, LUCA A D, VO N Q, DUNAND D C, LEINENBACH C. Coarsening- and creep-resistance of precipitation-strengthened Al−Mg−Zr alloys processed by selective laser melting [J]. Acta Materialia, 2020, 188: 192−202.

[19] SCHLIEPHAKE D, BAYOUMY D, SEILS S, SCHULZ C, KAUFFMANN A, WU X, HUANG A J. Mechanical behavior at elevated temperatures of an Al−Mn−Mg−Sc−Zr alloy manufactured by selective laser melting [J]. Materials Science and Engineering A, 2022, 831: 142032.

[20] SCHMIDTKE K, PALM F, HAWKINS A, EMMELMANN C. Process and mechanical properties: Applicability of a scandium modified Al-alloy for laser additive manufacturing [J]. Physics Procedia, 2011, 12: 369−374.

[21] SPIERINGS A B, DAWSON K, KERN K, PALM F, WEGENER K. SLM-processed Sc- and Zr-modified Al−Mg alloy: Mechanical properties and microstructural effects of heat treatment [J]. Materials Science and Engineering A, 2017, 701: 264−273.

[22] JIA Qing-bo, ZHANG Fan, ROMETSCH P, LI Jing-wei, MATA J, WEYLAND M, BOURGEOIS L, SUI Man-ling, WU Xin-hua. Precipitation kinetics, microstructure evolution and mechanical behavior of a developed Al−Mn−Sc alloy fabricated by selective laser melting [J]. Acta Materialia, 2020, 193: 239−251.

[23] JIA Qing-bo, ROMETSCH P, KÜRNSTEINER P, CHAO Qi, HUANG Ai-jun, WEYLAND M, BOURGEOIS L, WU Xin-hua. Selective laser melting of a high strength Al−Mn−Sc alloy: Alloy design and strengthening mechanisms [J]. Acta Materialia, 2019, 171: 108−118.

[24] LI Rui-di, WANG Min-bo, LI Zhi-ming, CAO Peng, YUAN Tie-chui, ZHU Hong-bin. Developing a high-strength Al−Mg−Si−Sc−Zr alloy for selective laser melting: Crack-inhibiting and multiple strengthening mechanisms [J]. Acta Materialia, 2020, 193: 83−98.

[25] TANG Hao, GENG Yao-xiang, BIAN Shu-nuo, XU Jun-hua, ZHANG Zhi-jie. An ultra-high strength over 700 MPa in Al−Mn−Mg−Sc−Zr alloy fabricated by selective laser melting [J]. Acta Metallurgica Sinica (English Letters), 2022, 35: 466−474.

[26] GENG Yao-xiang, TANG Hao, XU Jun-hua, ZHANG Zhi-jie, XIAO Ya-kai, WU Yi. Strengthening mechanisms of high-performance Al−Mn−Mg−Sc−Zr alloy fabricated by selective laser melting [J]. Science China Materials, 2021, 64: 3131−3137.

[27] NOVOTNY G M, ARDELL A J. Precipitation of $Al_3Sc$ in binary Al−Sc alloys [J]. Materials Science and Engineering A, 2001, 318: 144−154.

[28] YUAN Wei-hao, CHEN Hui, CHENG Tan, WEI Qing-song. Effects of laser scanning speeds on different states of the molten pool during selective laser melting: Simulation and experiment [J]. Materials & Design, 2020, 189: 108542.

[29] ZHU Yi-xin, ZHAO Yang, CHEN Bin. A study on Sc- and Zr-modified Al−Mg alloys processed by selective laser melting [J]. Materials Science and Engineering A, 2022, 833: 142516.

[30] SHI Yun-jia, YANG Kun, KAIRY S K, PALM F, WU Xin-hua, ROMETSCH P A. Effect of platform temperature on the porosity, microstructure and mechanical properties of an Al−Mg−Sc−Zr alloy fabricated by selective laser melting [J]. Materials Science and Engineering A, 2018, 732: 41−52.

[31] ZHOU Li-bo, YUAN Tie-chui, LI Rui-di, TANG Jian-zhong, WANG Guo-hua, GUO Kai-xuan. Selective laser melting of pure tantalum: Densification, microstructure and mechanical behaviors [J]. Materials Science and Engineering A, 2017, 707: 443−451.

[32] LI X P, WANG X J, SAUNDERS M, SUVOROVA A, ZHANG L C, LIU Y J, FANG M H, HUANG Z H, SERCOMBE T B. A selective laser melting and solution heat treatment refined Al−12Si alloy with a controllable ultrafine eutectic microstructure and 25% tensile ductility [J]. Acta Materialia, 2015, 95: 74−82.

[33] BI Jiang, LEI Zheng-long, CHEN Yan-bin, CHEN Xi, TIAN Ze, LIANG Jing-wei, QIN Xi-kun. Densification, microstructure and mechanical properties of an Al−14.1Mg−0.47Si−0.31Sc−0.17Zr alloy printed by selective laser melting [J]. Materials Science and Engineering A, 2020, 774: 138931.

[34] GENG Yao-xiang, TANG Hao, XU Jun-hua, ZHANG Zhi-jie, YU Li-hua, JU Hong-bo, JIANG Le, JIAN Jiang-lin. Formability and mechanical properties of high strength Al−(Mn,Mg)−(Sc,Zr) alloy produced by selective laser melting [J]. Acta Metallurgica Sinica, 2022, 58: 1044−1054. (in Chinese)

[35] TANG Hao, GENG Yao-xiang, LUO Jin-jie, XU Jun-hua, JU Hong-bo, YU Li-hua. Mechanical properties of high Mg content Al−Mg−Sc−Zr alloy fabricated by selective laser melting [J]. Metals and Materials International, 2021, 27: 2592−2599.

[36] LI Qiu-ge, LI Gui-chuan, LIN Xin, ZHU Dai-man, JIANG Jin-hang, SHI Shuo-qing, LIU Feng-gang, HUANG Wei-dong, VANMEENSEL K. Development of a high strength Zr/Sc/Hf-modified Al−Mn−Mg alloy using laser

powder bed fusion: Design of a heterogeneous microstructure incorporating synergistic multiple strengthening mechanisms [J]. Additive Manufacturing, 2022, 57: 102967.
[37] BAKARE F, SCHIEREN L, ROUXEL B, JIANG L, LANGAN T, KUPKE A, WEISS M, DORIN T. The impact of $L1_2$ dispersoids and strain rate on the Portevin-Le-Chatelier effect and mechanical properties of Al−Mg alloys [J]. Materials Science and Engineering A, 2021, 811: 141040.
[38] YODER J K, GRIFFITHS R J, YU H Z. Deformation-based additive manufacturing of 7075 aluminum with wrought-like mechanical properties [J]. Materials & Design, 2021, 198: 109288.
[39] CROTEAR J R, GRIFFITHS S, ROSSELL M D, LEINEBACH C, KENEL C, JANSEN V, SEIDMAN D N, DUNAND D C, VO N Q. Microstructure and mechanical properties of Al−Mg−Zr alloys processed by selective laser melting [J]. Acta Materialia, 2018, 153: 35−44.
[40] GRIFFITHS S, ROSSELL M D, CROTEAU J, VO N Q, DUNAND D C, LEINENBACH C. Influence of laser rescanning on the microstructure of a SLM processed Al−Mg−Zr alloy [J]. Materials Characterization, 2018, 143: 34−42.
[41] WU H, WEN S P, WU X L, GAO K Y, HUANG H, WANG W, NIE Z R. A study of precipitation strengthening and recrystallization behavior in dilute Al−Er−Hf−Zr alloys [J]. Materials Science and Engineering A, 2015, 639: 307−313.
[42] LENG Jin-feng, REN Bing-hui, ZHOU Qing-bo, ZHAO Ji-wei. Effects of Sc and Zr on recrystallization behavior of 7075 aluminum alloy [J]. Transactions of Nonferrous Metals Society of China, 2021, 31: 2545−2557.
[43] WANG Qing, LI Zhen, PANG Shu-jie, LI Xiao-na, DONG Chuang, LIAW P K. Coherent precipitation and strengthening in compositionally complex alloys: A review [J]. Entropy, 2018, 20: 878−900.
[44] ZHU Zhi-guang, NG F L, SEET H L, LU Wen-jun, LIEBSCHER C H, RAO Zi-yuan, RAABE D, NAI S M L. Superior mechanical properties of a selective-laser-melted AlZnMgCuScZr alloy enabled by a tunable hierarchical microstructure and dual-nanoprecipitation [J]. Materials Today, 2022, 52: 90−101.
[45] UESUGI T, HIGASHI K. First-principles studies on lattice constants and local lattice distortions in solid solution aluminum alloys [J]. Computational Materials Science, 2013, 67: 1−10.
[46] KIMURA T, NAKAMOTO T, OZAKI T, SUGITA K, MIZUNO M, ARAKI H. Microstructural formation and characterization mechanisms of selective laser melted Al−Si−Mg alloys with increasing magnesium content [J]. Materials Science and Engineering A, 2019, 754: 786−798.
[47] RYEN Ø, HOLMEDAL B, NIJS O, NES E, SJÖLANDER E, EKSTRÖM H E. Strengthening mechanisms in solid solution aluminum alloys [J]. Metallurgical and Materials Transactions A, 2006, 37: 1999−2006.
[48] YANG K V, SHI Yun-jia, PALM F, WU Xin-hua, ROMETSCH P. Columnar to equiaxed transition in Al−Mg(−Sc)−Zr alloys produced by selective laser melting [J]. Scripta Materialia, 2018, 145: 113−117.
[49] BURANOVA Y, KULITSKIY V, PETERLECHNER M, MOGUCHEVA A, KAIBYSHEV R, DIVINSKI S V, WILDE G. $Al_3(Sc,Zr)$-based precipitates in Al−Mg alloy: Effect of severe deformation [J]. Acta Materialia, 2017, 124: 210−224.
[50] KÜRNSTEINER P, BAJAJ P, GUPTA A, WILMS M B, WEISHEIT A, LI X S, LEINENBACH C, GAULT B, JÄGLE E A, RAABE D. Control of thermally stable core-shell nano-precipitates in additively manufactured Al−Sc−Zr alloys [J]. Additive Manufacturing, 2020, 32: 100910.
[51] GU Dong-dong, ZHANG Han, DAI Dong-hua, MA Cheng-long, ZHANG Hong-mei, LI Yu-xin, LI Shu-hui. Anisotropic corrosion behavior of Sc and Zr modified Al−Mg alloy produced by selective laser melting [J]. Corrosion Science, 2020, 170: 108657.

# 激光粉末床熔融成形高性能 Al−Mn−Mg−Sc−Zr 合金的显微组织演变及力学性能

唐 浩[1]，耿遥祥[2]，高超峰[3]，席晓莹[1]，张建涛[1]，肖志瑜[1]

1. 华南理工大学 国家金属材料近净成形工程技术研究中心，广州 510640；
2. 江苏科技大学 材料科学与工程学院，镇江 212003；
3. 季华实验室 先进增材制造研究所，佛山 528200

**摘 要：**系统研究时效温度对激光粉末床熔融成形 Al−Mn−Mg−Sc−Zr 合金显微组织及力学性能的影响。结果表明，成形态合金组织致密且无裂纹，平均晶粒尺寸为 3.51 μm，屈服强度为(547±3) MPa。经 300 ℃时效后，合金组织中析出大量尺寸为 2~3 nm 且与基体共格的 $Al_3Sc$ 纳米颗粒。时效样品的屈服强度提升至(616±4) MPa，这得益于合金中的析出强化、固溶强化和晶界强化。当时效温度超过 300 ℃时，部分 Mn 和 Zr 从固溶体中析出，形成 $Al_6Mn$ 和 $Al_3(Sc,Zr)$相。经 500 ℃时效后，合金中 $Al_6Mn$ 相和 $Al_3(Sc,Zr)$相分别粗化至约 600 和 30 nm。因此，合金的屈服强度下降至(372±3) MPa。

**关键词：**激光粉末床熔融；Al−Mn−Mg−Sc−Zr 合金；显微组织演变；力学性能；$Al_3Sc$ 纳米颗粒

**(Edited by Wei-ping CHEN)**